ACS APPLIED ENERGY MATERIALS

www.acsaem.org Article

Enhancing Efficiency in Dye-Sensitized Solar Cells: Incorporation of Cu_3VSe_4 Nanocrystals into TiO_2 Photoanodes

Navdeep Kaur, Linisha Biswal, Alexander Prieto, Cheng-Yu Lai, and Daniela R. Radu*

Cite This: https://doi.org/10.1021/acsaem.4c00911 Read Online

ACCESS | Metrics & More | Article Recommendations | Supporting Information

ABSTRACT: In the quest for sustainable energy solutions to meet the growing energy demands, third-generation solar photovoltaic (PV) technologies, specifically dye-sensitized solar cells (DSSCs), have gained considerable attention for their cost-effectiveness, ease of manufacture, and operability under dim-light conditions. However, the limited light-harvesting capability of mesoporous titanium dioxide (m-TiO_2) photoanodes presents a significant hurdle, constraining the power conversion efficiency (PCE) of the DSSCs. The present work introduces a class of semiconducting materials known as sulvanites, with a particular focus on Cu_3VSe_4, which is aimed at addressing the light-harvesting issues encountered with m-TiO_2. Cu_3VSe_4 exhibits a broad absorption across the visible range of solar spectrum, which substantially enhances light absorption in DSSCs, when incorporated into m-TiO_2 photoanodes. Cu_3VSe_4 nanocrystals, synthesized via a hot injection, one-pot synthesis method, are incorporated in m-TiO_2 (Cu_3VSe_4/m-TiO_2) via direct chemical mixing. To understand the induced changes in the structural and optical properties of m-TiO_2 by incorporating Cu_3VSe_4 nanocrystals, the prepared thin films are characterized using scanning electron microscopy (SEM), Brunauer–Emmett–Teller (BET), attenuated total reflectance (ATR), UV–vis, and Raman spectroscopy. DSSCs employing Cu_3VSe_4/m-TiO_2 photoanodes demonstrated a noteworthy 14.28% increase in PCE (reaching 7.38%) compared to that of reference m-TiO_2 DSSCs (6.37%). The enhanced PCE is attributed to the improved light absorption of photoanodes resulting from enhanced porosity and dye-loading content of Cu_3VSe_4/m-TiO_2 photoanodes and improved charge-transfer processes. The improved charge-transport kinetics of fabricated DSSCs is confirmed from the reduced resistances at different interfacial layers estimated from the electrochemical impedance spectroscopy (EIS) spectra. Furthermore, external quantum efficiency (EQE) spectra indicate an improved spectral response of Cu_3VSe_4/m-TiO_2 photoanodes in DSSCs. Hence, the incorporation of sulvanites offers a promising strategy to enhance the light-harvesting efficiency not only in DSSCs but also in various cutting-edge optoelectronic devices.

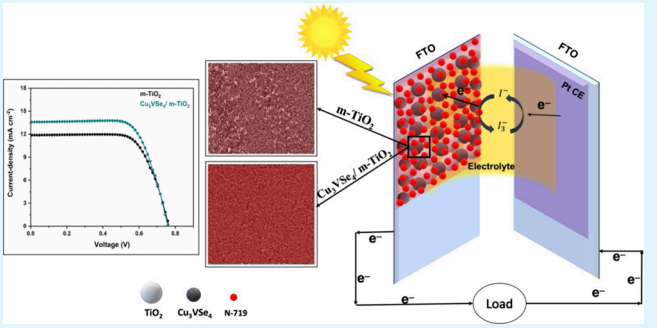

KEYWORDS: *sulvanite, Cu_3VSe_4, light-harvesting, photogenerated electrons, dye-sensitized solar cells, external quantum efficiency*

INTRODUCTION

Over the past few decades, solar photovoltaic (PV) technologies have gotten significant attention as renewable energy producers. Third-generation PV devices, particularly dye-sensitized solar cells (DSSCs), have been attractive due to their cost-effective components, flexible and lightweight design, high transparency, eco-friendliness, efficient charge carrier mechanism, and better performance in dim-light conditions when compared to other solar PV technologies.[1−3] This makes DSSC a competent contender not only in replacing commercial silicon solar cells but also toward building integrated photovoltaic and agrivoltaic applications.[4,5] Typically, a DSSC consists of a mesoporous semiconductor photoanode sensitized with dye molecules, namely a photoanode, a platinum (Pt) counter electrode (CE), and a redox electrolyte.[6] Despite DSSC's maturity, its highest certified power conversion efficiency (PCE) stands at only 13% and depends on the following factors: (1) light absorption efficiency, (2) charge injection efficiency, and (3) charge collection efficiency. Although all the components of DSSCs contribute collectively to improving the PCE, the nanostructured mesoporous semiconductor material in photoanodes plays a significant role as an electron transport layer (ETL).[7] It provides a pillar for dye adsorption responsible for incident light absorption, accepting electrons from the excited state of the dye and transporting electrons toward the Pt CE. So far, among different semiconducting materials like ZnO,

Received: April 10, 2024
Revised: May 18, 2024
Accepted: May 22, 2024

https://doi.org/10.1021/acsaem.4c00911
ACS Appl. Energy Mater. XXXX, XXX, XXX−XXX

SnO_2, Nb_2O_5, and so forth, mesoporous TiO_2 (m-TiO_2) has been considered as one of the best choices for ETL in DSSCs due to its nontoxic nature, high refractive index, biocompatibility, high transparency toward visible light, chemical and thermal stability, facile synthesis, and low cost.[8] However, m-TiO_2 suffers from a higher recombination reaction rate due to the relatively slow charge transport, the tendency to agglomerate, and poor absorption in the visible region of the solar spectrum due to its wide band gap (~3.2 eV), thus limiting the PCE of DSSCs. It has been well established that these limitations can be resolved by surface engineering of m-TiO_2; to this end, the incorporation of enhancing nanoparticles is considered the most effective way, by offering relatively large surface area for adsorption and modulating its binding strengths toward enhanced dye adsorption, hence improving the current densities and charge transport in DSSCs. To date, various nanoparticles have been explored, including transition-metal dichalcogenides, carbonaceous materials, and so forth; however, their impact was not substantial.[9,10] The research findings on modified TiO_2 using different materials in DSSCs based on the changes induced in their PCE are summarized in Table 1.

Table 1. PCE of Various Nanostructures Incorporated in TiO_2 for DSSCs

photoanode material	%PCE	reference
TiO_2/plasmonic gold nanoparticles	2.72	11
AgNPs-TiO_2 film	4.69	12
Co-/rGO-codoped TiO_2	5.24	13
WO_3/TiO_2	5.29	14
TiO_2 + 5 wt % $Ag_{0.2}Zn_{0.90}Fe_2O_4$	5.75	15
TiO_2NS/GO/g-C_3N_4	5.77	16
$PbTiO_3$−$ZnFe_2O_4/TiO_2$	5.87	17
AgNWs@TiO_2	5.88	18
AC/TiO_2−$SrTiO_3$	5.90	19
Fe-doped TiO_2 hollow spheres	6.02	20
NiO@f-MWCNT-TiO_2	6.50	21
rGO-modified TiO_2	6.52	22
Cu-doped TiO_2	6.94	23
Y^{3+}-TiO_2	6.88	24
Cu_3VSe_4/m-TiO_2	7.28	present work

Toward this direction, the family of sulvanites, i.e., ternary copper chalcogenide (Cu_3MX_4 (M = V, Nb, or Ta; X = S, Se, or Te)), possessing unique crystal structure, optical and electronic properties, and good electrical conductivities, has emerged.[25−28] Most sulvanites are sustainable, as they are composed of nontoxic and Earth-abundant elements. Nanoscale sulvanites have emerged in recent years as well suited for optoelectronic applications. Zhao et al. reported the synthesis of cube-shaped Cu_3NbSe_4 nanocrystals with high crystallinity, uniformity, and monodispersity using a facile method. It demonstrates the optoelectronic properties of Cu_3NbSe_4, showing its potential for application in electronics and optoelectronics, particularly as a photoactive material with a higher light-to-dark current ratio (I_{light}/I_{dark}) representing strong sensitivity toward incident light giving broad spectral light-harvesting ability, fast response speeds, and excellent stability.[29] We successfully demonstrated the ability to fine-tune the Cu_3VSe_4 nanocrystal particle size in the range of ~25 to 30 nm by tailoring the amount of surfactant utilized in the synthesis. While absorbance is in the UV−visible region of the solar spectrum, the particle size impacts the Cu_3VSe_4-specific absorbance wavelength, enabling the rational design of particles with desired optical properties.[30]

The present work investigates the effect of Cu_3VSe_4 nanocrystals, with a particle size of ~30 nm, on the light-harvesting properties of photoanodes in DSSCs. The impact of the incorporation of Cu_3VSe_4 on the structural and optical properties of m-TiO_2 was evaluated. Cu_3VSe_4 nanocrystals incorporated in m-TiO_2 (Cu_3VSe_4/m-TiO_2) were used to fabricate photoanodes in DSSCs, and the PV parameters were obtained from the photocurrent density−voltage curves. The charge-transport kinetics describing the improved PV performance of Cu_3VSe_4/m-TiO_2 DSSCs as compared to m-TiO_2 DSSC were determined through electrochemical impedance spectroscopy (EIS) measurements. The external quantum efficiency (EQE) measurements of the fabricated DSSCs were used to verify their spectral absorption variation based on the modified TiO_2 photoanodes.

EXPERIMENTAL SECTION

Chemicals. Copper(I) chloride (CuCl, 99%), 1-dodecanethiol (1-DDT, 98%), selenium powder (Se, 99.99%), oleylamine (OLA, 70%), and methyl acetate (MeOAc, anhydrous, 99.5%) were purchased from Sigma-Aldrich; vanadium(IV) oxide acetylacetonate ($VO(acac)_2$, ≥ 98%), ethanol (EtOH, anhydrous), chloroform ($CHCl_3$, 99.9%), and potassium hydroxide (KOH) were purchased from Thermo Fisher. For the fabrication of DSSCs, fluorine-doped tin oxide (FTO) substrates were purchased from Hartford Glass Co., Inc.; EL-HSE electrolyte and ditetrabutylammonium cis-bis(isothiocyanato)bis-(2,2′-bipyridyl-4,4′-dicarboxylato) ruthenium(II) (N719) dye were obtained from Greatcell Solar Co., Ltd. (Queanbeyan, AU); Platisol-T from Solaronix (Aubonne, CH)); zinc powder, titanium(IV) isopropoxide (TTIP), and titanium dioxide (TiO_2) paste were purchased from Sigma-Aldrich (Saint Louis, MI).

Synthesis of Cu_3VSe_4 Nanocrystals. The synthesis procedure follows our reported methodology.[30] In a typical experiment, CuCl (220 mg, 2.2 mmol), $VO(acac)_2$ (265 mg, 1 mmol), Se (240 mg, 3 mmol), OLA (20 mL), and 1-DDT (0.25 mL) were added to a 250 mL round-bottom flask. The Schlenk line technique was used for the synthesis of Cu_3VSe_4 nanocrystals. The mixture was initially degassed at 120 °C under vacuum for 30 min. After degassing, the reaction mixture was heated to 260 °C and kept at this temperature for 2 h. The reaction mixture was then allowed to cool naturally, followed by purification. The nanoparticles were washed by using a $CHCl_3$/EtOH (1:3) solvent pair three times and collected by centrifugation. Subsequently, ligand exchange was conducted using MeOAc. To the resulting mixture was added $CHCl_3$/MeOAc (1:3), followed by centrifugation. A dispersion (ink) was prepared by redispersing the Cu_3VSe_4 nanocrystals in $CHCl_3$ (~5 mL).

Preparation of Photoanodes. Photoanodes were fabricated by following a multistep procedure reported in our work.[31,32] The FTO substrates were first patterned using a chemical etching procedure, which involved depositing zinc paste on the FTO layer and then etching it with an aqueous HCl (18.5% v/v) solution added dropwise. The substrates were then rinsed with nanopure water. Following this, the patterned substrates underwent a thorough cleaning process, involving the following steps: (1) immersion in a soap solution of Hellmanex III in nanopure water (2% v/v), (2) rinsing with nanopure water and then washing with (3) acetone, (4) ethanol, and (5) isopropanol, and heated to 80 °C. At each step, the substrates were subjected to ultrasonication for 15 min and then dried in N_2 flow. After cleaning, the FTO substrates were ozone-treated with an Ossila UV ozone cleaner for 30 min to eliminate any remaining organic surface contaminants. The treated FTO substrates were then placed on a hot plate and heated for several minutes until they reached a target temperature of 450 °C. Once this temperature was achieved, a layer of c-TiO_2 was deposited onto the heated substrates by spraying a

https://doi.org/10.1021/acsaem.4c00911
ACS Appl. Energy Mater. XXXX, XXX, XXX−XXX

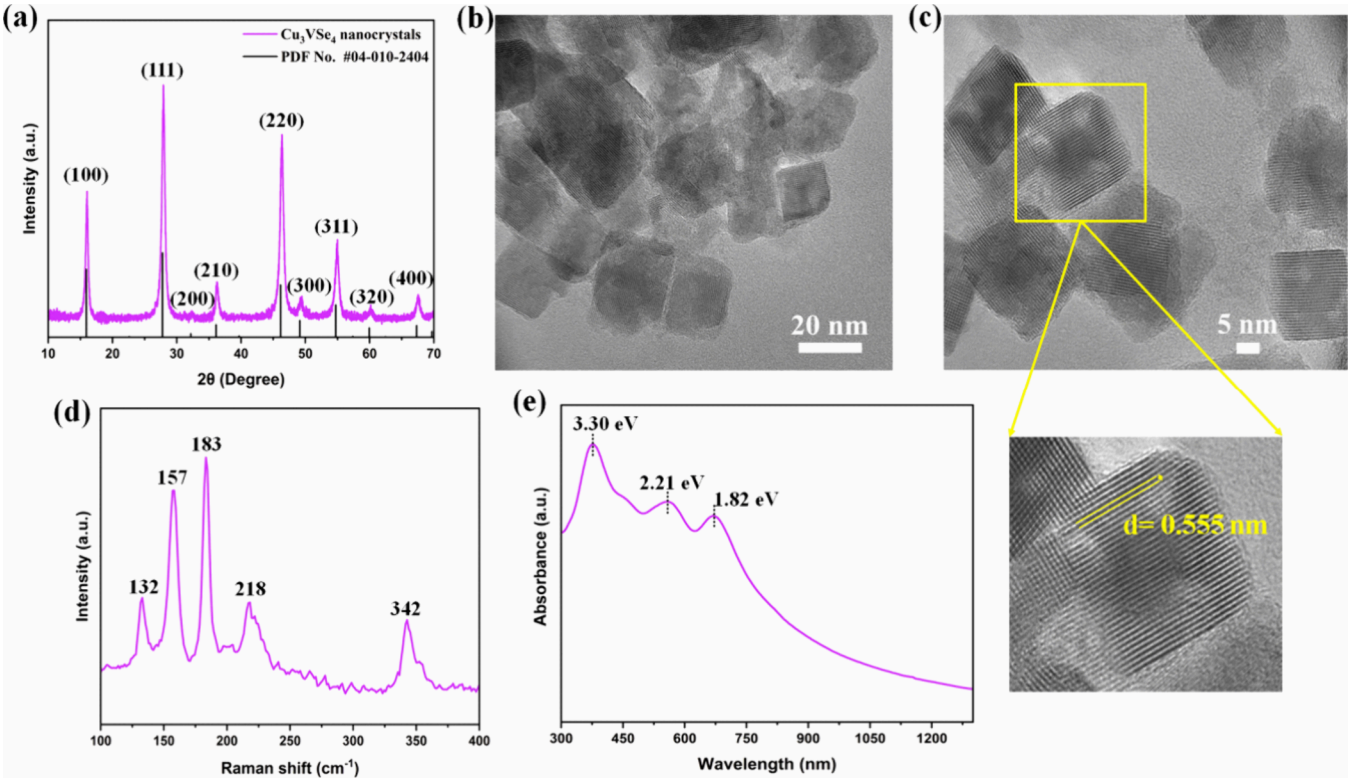

Figure 1. (a) XRD pattern of Cu_3VSe_4 nanocrystals along with its reference pattern (PDF No. #04-010-2404) obtained from the ICDD database. (b) Low-magnification and (c) high-magnification TEM images of Cu_3VSe_4 nanocrystals with a zoomed view of lattice fringes showing an interplanar spacing of 0.555 nm corresponding to the (100) crystal plane, (d) Raman spectra, and (e) UV−visible absorbance spectra of Cu_3VSe_4 nanocrystals dissolved in the chloroform solvent.

0.4 M solution of TTIP in ethanol. The coated substrates were kept at this temperature for 30 min and then cooled to room temperature. Subsequently, two types of photoanodes were prepared. First, a commercial TiO_2 paste was doctor-bladed onto c-TiO_2 deposited FTO substrates (c-TiO_2/FTO) to prepare a mesoporous TiO_2 (m-TiO_2) film for reference purpose in DSSCs. Second, the synthesized Cu_3VSe_4 nanocrystals incorporated in commercial TiO_2 paste (0.055, 0.045, and 0.035 w/w) was doctor-bladed on c-TiO_2/FTO to obtain Cu_3VSe_4/ m-TiO_2 films with varied amounts of Cu_3VSe_4 nanocrystals. It is to be noted that the thickness and the effective area for both the m-TiO_2 and Cu_3VSe_4/m-TiO_2 films were kept the same, which are ∼11.5 μm and 0.15 cm^2, respectively. The prepared films of m-TiO_2/c-TiO_2/FTO and Cu_3VSe_4 incorporated with m-TiO_2/c-TiO_2/FTO were then annealed at 450 °C for 30 min. Finally, these substrates were immersed in a N719 dye solution (0.4 mM in ethanol) for a duration of 20 h, resulting in desired photoanodes.

Preparation of Counter Electrodes. A Pt reference CE is prepared as follows: 60 μL of Platisol-T was drop-casted onto precleaned FTO substrates, as mentioned in the photoanode preparation section, and then annealed at 450 °C for 30 min.

DSSC Assembly. DSSCs were fabricated by assembling the photoanode and CE in a sandwich-type geometry. An electrolyte containing the redox couple I^-/I_3^- was introduced in between them to close the circuit.

Characterizations. PV testing was carried out at an incident power intensity of 100 mW/cm^2 (under 1 sun illumination or AM 1.5G) using an ORIEL LCS-100TM solar simulator. For accuracy of the data, a silicon solar cell was used to calibrate the solar simulator. Using an Ω Metrohm Autolab system, electrochemical impedance spectroscopy (EIS) measurements were performed at a frequency range of 0.1 Hz to 1 MHz. External quantum efficiency (EQE) measurements were performed with an Enlintech QE-R system equipped with a xenon lamp, within the wavelength range of 300−750 nm and keeping the chopper frequency to a minimum value of 10 Hz. Prior to taking EQE measurements, the instrument was calibrated using a standard silicon solar cell. UV−vis-NIR measurements were collected by using a Shimadzu UV-3600 Plus spectrophotometer. The JEOL/JSM-F100 Schottky field emission SEM instrument was utilized to investigate the surface morphology. A Quantachrome NOVA touch LX-2 (Anton Parr, Texas, USA), Brunauer−Emmett−Teller (BET) instrument was used to obtain the specific surface area and the pore volumes of m-TiO_2 and Cu_3VSe_4/m-TiO_2 from N_2 adsorption−desorption isothermal curves. A Shimadzu/IRTracer-100 instrument equipped with an attenuated total reflectance (ATR) unit was used to perform Fourier transform infrared (FT-IR) spectroscopy. Raman measurements were conducted on a WITec Alpha 300 Raman microscope with a 532 nm laser. The PL emission spectra of the prepared photoanodes were collected with an Edinburgh Instruments FS5 spectrofluorometer. X-ray diffraction (XRD) patterns were obtained from a Rigaku MiniFlex system with a Cu Kα radiation source (λ = 1.5405 Å) operated at 40 mV and 30 mA. High-resolution transmission electron microscopy (HR-TEM) images were captured using a 200 kV JEOL JEM-2100 Plus instrument.

RESULTS AND DISCUSSION

Characterization of Cu_3VSe_4 Nanocrystals. The structural and spectroscopic characterization of Cu_3VSe_4 nanocrystals unveils their intrinsic properties and optical profiles, as depicted in Figure 1. The XRD pattern of Cu_3VSe_4 nanocrystals depicted in Figure 1a exhibits diffraction peaks at 16.05, 27.88, 32.32, 36.21, 46.38, 49.29, 54.92, 60.17, and 67.38° Bragg's angles relating to the (100), (111), (200), (210), (220), (300), (311), ($\bar{3}$20), and (400) crystal planes of cubical structure, with the $P\bar{4}3m$ space group matching the reference (database PDF No. #04-010-2404).[30] The sharp peaks in the diffraction pattern indicate the good crystallinity of Cu_3VSe_4 nanocrystals. The *d*-spacing of 0.551 nm

https://doi.org/10.1021/acsaem.4c00911
ACS Appl. Energy Mater. XXXX, XXX, XXX−XXX

corresponding to the (100) crystal plane was estimated from the XRD peak at 16.05° Bragg's angle. The cubic structure of Cu_3VSe_4 nanocrystals is also observed from the morphological investigations through low-magnification TEM images, as depicted in Figure 1b, with an average particle size of ∼30 nm. Further, high-resolution TEM images (Figure 1c) depict the *d*-spacing of 0.555 nm corresponding to the (100) crystal planes, which is in agreement with the XRD estimation. The Raman spectra of synthesized Cu_3VSe_4 nanocrystals are depicted in Figure 1d, and the presence of Raman active modes around 132, 157, 183, 217, and 342 cm^{-1} seems to be consistent with the reported literature.[33,34] The peaks at 132 and 342 cm^{-1} relate to the F_2^a and F_2^d vibrational modes of the Cu_3VSe_4 nanocrystal, respectively.[35] Figure 1e depicts the optical UV−visible absorption spectra of Cu_3VSe_4 nanocrystals, indicating three absorption bands around 375, 561, and 678 nm. These bands are related to VB-CB (3.30 eV), VB-IB I (2.21 eV), and VB-IB II (1.82 eV), respectively, which is in close agreement with other reported studies.[34,36]

Concept Visualization. Figure 2 illustrates the hypothesis behind improving the PV performance of DSSC by incorporating Cu_3VSe_4 in m-TiO_2 photoanodes. In the reference m-TiO_2 DSSC, when incident light strikes the glass side of the photoanode's FTO substrate, it penetrates through the compact TiO_2 (c-TiO_2) and m-TiO_2 layers, thereby exciting N719 dye-sensitizer molecules and generating excitons. The difference in energy levels between the lowest unoccupied molecular orbital (LUMO) of N719 dye and the conduction band (CB) of m-TiO_2 facilitates the separation of these excitons, with the electrons migrating toward the m-TiO_2 layer becoming photogenerated electrons or charge carriers. These photogenerated electrons proceed through the c-TiO_2 layer, entering the external circuit via the conducting FTO substrate, and ultimately reaching the Pt CE. At the Pt CE and electrolyte interface, the reduction of triiodide ions (I_3^-) to iodide ions (I^-) takes place, which diffuse toward the photoanodes, thereby facilitating the regeneration of the N719 dye sensitizer through the oxidation of I^- to I_3^-. This process aids in converting incident light into electrical energy by the DSSC. However, a significant hurdle in this process lies in the limited light-harvesting capacity of photoanodes along with the recombination reactions occurring at the photoanode/electrolyte interface, which ultimately diminishes the PCE of DSSCs.

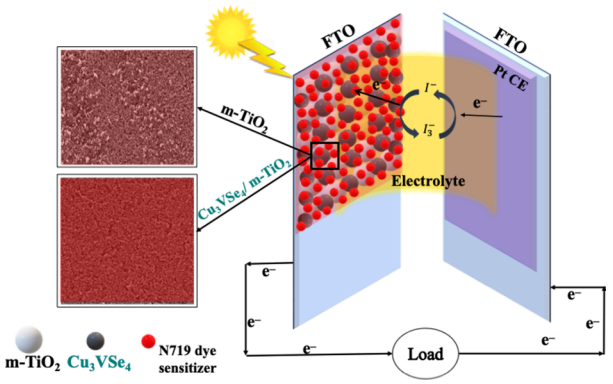

Figure 2. Schematic representation of Cu_3VSe_4-induced changes in m-TiO_2 as photoanodes for DSSC.

The Cu_3VSe_4 incorporation in m-TiO_2 photoanodes in DSSCs is hypothesized to address these challenges. Since the absorbance of Cu_3VSe_4 nanocrystals lies within the UV−visible absorbance range from 300 to 800 nm, it is expected to amplify the incident light absorbance of N719 dye-loaded photoanodes when incorporated in m-TiO_2. Thus, higher absorbance with the incorporation of Cu_3VSe_4 nanocrystals might aid in improving the light-harvesting capability of photoanodes in DSSCs. The higher light absorbance of photoanodes results in the generation of an increased number of photogenerated electrons, which participate in generating larger current densities in the DSSC. Larger current densities result in a higher PCE of DSSCs. Furthermore, considering the conductive nature of Cu_3VSe_4 nanocrystals, it facilitates the swift transport of photogenerated electrons from the highest occupied molecular orbital (HOMO) of the N719 dye to the CB of m-TiO_2, thus comparatively reducing the recombination reaction at the photoanode/electrolyte interface. This augmentation in the light-harvesting capability of photoanodes and improved charge-transport kinetics is expected to significantly improve the overall PV performance of DSSCs employing modified Cu_3VSe_4/m-TiO_2 photoanodes.

Optimization of Amount of Cu_3VSe_4 Nanocrystals in m-TiO_2 Photoanodes for High-Performance DSSCs. To validate our hypothesis, we examined the impact of incorporating Cu_3VSe_4 nanocrystals in m-TiO_2 photoanodes on the PV performance of the DSSCs. The PV performance of the fabricated DSSCs was evaluated from the current density−voltage (*J*−*V*) characteristics obtained under a light illumination with power intensity of 100 mW cm^{-2} (AM 1.5 G) in terms of calculated PV parameters, namely short-circuit current−density (J_{SC}), open-circuit voltage (V_{OC}), fill factor (FF), and PCE.

The effect of the concentration of Cu_3VSe_4 nanocrystals on the PV performance of DSSCs was investigated by incorporating different amounts of Cu_3VSe_4 (0.055, 0.045, and 0.035 w/w) nanocrystals in m-TiO_2 photoanodes. For comparison purposes, a reference DSSC was fabricated using an m-TiO_2 photoanode. Five devices were fabricated using each type of photoanode, i.e., m-TiO_2 and Cu_3VSe_4/m-TiO_2 (0.055, 0.045, and 0.035 w/w). Figure S1 depicts the *J*−*V* curves of the champion devices, and their PV parameters are tabulated in Table S1. The PCE trend of different concentrations of Cu_3VSe_4 in m-TiO_2 based fabricated DSSCs is observed to be 0.045 w/w (7.28%) > 0.055 w/w (7.06%) > 0.035 w/w (6.90%) > reference m-TiO_2 (6.38%). A similar trend is observed in J_{SC} values for all the fabricated DSSCs (0.045 w/w (13.59 mA cm^{-2}) > 0.055 w/w (13.03 mA cm^{-2}) > 0.035 w/w (12.91 mA cm^{-2}) > m-TiO_2 (11.55 mA cm^{-2})), with a negligible change in the V_{OC} values (∼0.76 V). A slight decrease in the FF is observed in Cu_3VSe_4-modified DSSCs, with a further decrease trend from 0.055 to 0.035 w/w Cu_3VSe_4/m-TiO_2 photoanodes. The improved PV performance of Cu_3VSe_4/m-TiO_2 DSSCs relative to the reference m-TiO_2 DSSC could be attributed to the improved light-harvesting capabilities of the modified m-TiO_2 photoanodes, due to the synergistic effect of Cu_3VSe_4 nanocrystals and N719 dye molecules on the absorbance in the UV−visible spectral range. Among the different concentrations of Cu_3VSe_4/m-TiO_2, the lower concentration (0.035 w/w) did not show a comparatively higher PV performance in DSSCs, which might be due to the comparatively negligible change in light harvesting, and hence smaller J_{SC}, whereas the higher

https://doi.org/10.1021/acsaem.4c00911
ACS Appl. Energy Mater. XXXX, XXX, XXX−XXX

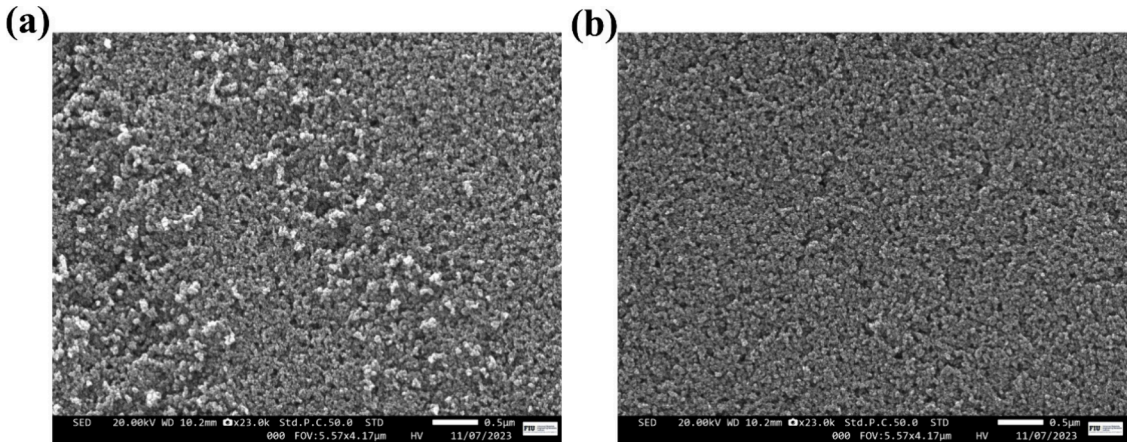

Figure 3. SEM images of (a) m-TiO_2 and (b) Cu_3VSe_4/m-TiO_2 (0.045 w/w) films doctor-bladed on FTO glass substrates with thickness ~11.5 μm.

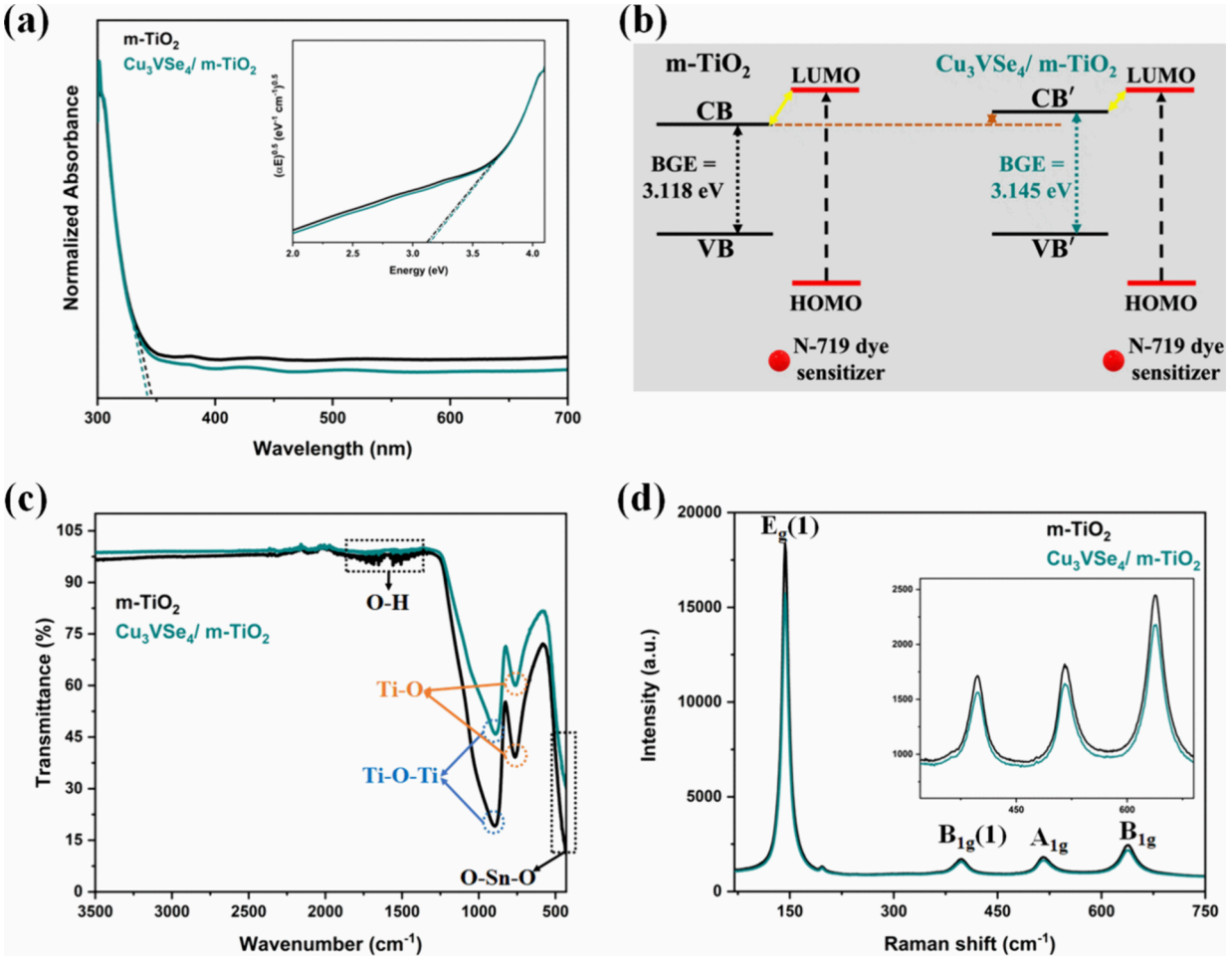

Figure 4. (a) UV absorbance spectra with the respective Tauc's plot (Inset) of m-TiO_2 and Cu_3VSe_4/m-TiO_2 (0.045 w/w). (b) Increased band gap energy (BGE) diagram of Cu_3VSe_4/m-TiO_2 relative to m-TiO_2*. (c) ATR and (d) Raman spectra of m-TiO_2 and Cu_3VSe_4/m-TiO_2 (0.045 w/w). CB, conduction band; VB, valence band; LUMO, lowest unoccupied molecular orbital; HOMO, highest occupied molecular orbital.

concentration (0.055 w/w) could lead to the presence of agglomerated Cu_3VSe_4 nanocrystals in m-TiO_2. This agglomeration, in turn, diminishes the conductivity, consequently resulting in comparatively lower J_{SC} and PCEs in the modified DSSCs. Thus, 0.045 w/w Cu_3VSe_4/m-TiO_2 photoanodes provided optimal PV performance in DSSCs. Hence, we concluded that when the concentration of Cu_3VSe_4 nanocrystals exceeds a certain threshold level, it can negatively impact on the performance of DSSC. We selected the optimal 0.045 w/w−Cu_3VSe_4/m-TiO_2 photoanodes to further evaluate the structural (SEM, BET, and XRD), optical (UV, Raman, and ATR), and photovoltaic (J−V, EIS, and EQE measurements) performance of the reference m-TiO_2 and the optimized 0.045 w/w Cu_3VSe_4/m-TiO_2 photoanode-based DSSCs.

https://doi.org/10.1021/acsaem.4c00911
ACS Appl. Energy Mater. XXXX, XXX, XXX−XXX

Morphological and Optical Properties of Cu_3VSe_4-Incorporated m-TiO_2: Insights and Findings. The impact of incorporating 0.045 w/w Cu_3VSe_4 on the morphology, surface uniformity, porosity, band gap, crystallinity, defects, and transmittance of m-TiO_2 was evaluated as follows. Figure 3 illustrates the SEM images of m-TiO_2 and Cu_3VSe_4/m-TiO_2 films doctor-bladed on FTO substrates. The film thickness of 11.5 μm is estimated from the cross-sectional SEM images as reported in our previous work.[37] The SEM images were acquired from the top surface of the films, which showed a continuous and uniform structure, indicating the high quality of the prepared photoanodes for DSSCs. The morphology of m-TiO_2 (Figure 3a) consists of randomly interconnected spherical nanoparticles forming a mesoporous surface, along with having a noticeable nanoparticle agglomeration on its surface, thus lacking apparent order in their pore arrangement. The uniformity of the m-TiO_2 film seems to be improved with the incorporation of Cu_3VSe_4 nanocrystals (Figure 3b), accompanied by negligible agglomerations showing uniform pore distribution as well. The Cu_3VSe_4 nanocrystal incorporation in m-TiO_2 is evidenced by EDS spectra and the respective elemental mapping images of m-TiO_2 (Figure S2) and Cu_3VSe_4/m-TiO_2 (Figure S3). While m-TiO_2 contains titanium (Ti) and oxygen (O) elements, the EDS of Cu_3VSe_4/m-TiO_2 shows the additional presence of copper (Cu), vanadium (V), and selenium (Se) elements alongside Ti and O elements (with traces of Sn originating from the FTO substrate in both samples).

Although SEM images qualitatively confirmed the improved surface uniformity and reduced surface agglomerations of Cu_3VSe_4/m-TiO_2, BET analysis was selected as a quantitative method for estimating the porosity and size of the photoanode pores. The N_2 adsorption desorption isotherms of m-TiO_2 and Cu_3VSe_4/m-TiO_2 photoanodes, along with the cumulative and differential pore volume distribution are shown in Figure S4. The isotherm curves belong to the H4 type of hysteresis loop with a broad pore size distribution, indicating mesoporous m-TiO_2 and Cu_3VSe_4/m-TiO_2. The specific surface area (S_{BET}) and pore volume of Cu_3VSe_4/m-TiO_2 improved from 69.51 to 81.796 $m^2\ g^{-1}$ and 0.4495 to 0.4786 cc g^{-1}, respectively, when compared with those of m-TiO_2. The reduction in nanoparticle agglomeration coupled with the improved uniformity and porosity of Cu_3VSe_4/m-TiO_2 is assumed to have the potential to enhance the light-harvesting capabilities of m-TiO_2 photoanodes in DSSCs.

The absorbance spectra can offer valuable insights into the optical characteristics of m-TiO_2 and modified Cu_3VSe_4/m-TiO_2 structures without dye loading and are depicted in Figure 4a. Both the films show firm absorption peaks around 300−400 nm with a negligible change in the absorbance in this region, indicating negligible change in the interaction of incident photons with m-TiO_2 even with the incorporation of Cu_3VSe_4 nanocrystals in this particular wavelength. It is important to note that there is a slight hypsochromic or blue shift in the absorption band edge of Cu_3VSe_4/m-TiO_2, which might indicate a slight increase in the band gap energy (BGE). BGE values for m-TiO_2 and Cu_3VSe_4/m-TiO_2 were evaluated from Tauc's plots (inset of Figure 4a) derived from the absorbance spectra and are found to be 3.118 and 3.145 eV, respectively. A slightly increased BGE value is attributed to the generation of few defect states in m-TiO_2 with the incorporation of Cu_3VSe_4 nanocrystals. The increased BGE of Cu_3VSe_4/m-TiO_2 reduces the energy barrier between the CB of m-TiO_2 and the HOMO level of N719 dye molecules (Figure 4b), which would be beneficial for the efficient transportation of photogenerated electrons in DSSCs, thus indirectly reducing the recombination reactions at the photoanode/electrolyte interface in DSSCs.[38] Thus, a slight increase in the BGE value of Cu_3VSe_4/m-TiO_2 is likely to improve the light-harvesting ability of m-TiO_2 photoanodes and hence the overall PV performance of DSSCs. The significant increase in BGE value is also detrimental as it could limit the absorption of lower-energy photons. Furthermore, the absorbance of Cu_3VSe_4/m-TiO_2 reduces in the visible region. It might be attributed to the improved uniformity of the m-TiO_2 surface seen from the SEM images. m-TiO_2 exhibits an intrinsic scattering effect due to its nonhomogeneous morphology. However, the surface of m-TiO_2 becomes more homogeneous with the incorporation of Cu_3VSe_4 nanocrystals, resulting in its comparatively reduced scattering effect and hence reduced absorbance. It is further benefiting for transmitting more incident photons lying within the visible spectral range toward the N719 dye molecules adsorbed on dye-sensitized Cu_3VSe_4/m-TiO_2 films, which would result in improved light absorption in the wavelength range 400−700 nm explained later.

Increased transmittance in Cu_3VSe_4/m-TiO_2 relative to that in m-TiO_2 is clearly depicted in the ATR spectra (Figure 4c). ATR spectra were taken on doctor-bladed m-TiO_2 and modified Cu_3VSe_4/m-TiO_2 films. In both samples, two broadened peaks around 760 and 890 cm^{-1} were observed in the wavenumber range 500−1000 cm^{-1}. It is attributed to a combination of Ti−O stretching vibrations (690.52 cm^{-1}), a characteristic peak of TiO_2, Sn−O stretching vibrations (642 cm^{-1}) of SnO_2 in FTO, and Ti−O−Ti stretching vibrations (924 cm^{-1}) of anatase TiO_2. A noisy signal appears in the wavenumber range from 1321 to 2420 cm^{-1} and is attributed to the rotational spectrum of water vapor present in the atmosphere. The ATR spectra begin with a dip around 495 cm^{-1} in both the films and are linked to the stretching vibrations of O−Sn−O.[39,40] The observed increase in the transmittance of Cu_3VSe_4/m-TiO_2 infers the changes induced in the bending modes of m-TiO_2 with the incorporation of Cu_3VSe_4, due to the comparatively decreased amount of m-TiO_2.

Figure 4d depicts the Raman spectra of m-TiO_2 and Cu_3VSe_4/ m-TiO_2 films. The observed four peaks of m-TiO_2 at 144 cm^{-1} having a shoulder at 197, 399, 518.9, and 639 cm^{-1} belong to the characteristic $E_g(1)$, $B_{1g}(1)$, A_{1g}, and B_{1g} modes, respectively.[41] The E_g mode represents the symmetric stretching vibrations of O−Ti−O bonds, and B_{1g} is the symmetric bending vibration and A_{1g} is the antisymmetric bending vibration of Ti−O bonds of the anatase phase of TiO_2.[41] Since all the Raman peaks are linked to the stretching or bending vibrations of Ti−O bonds, the slightly reduced Raman peak intensity in Cu_3VSe_4/m-TiO_2 might infer the breakdown of lattice periodicity and long-range translational crystal symmetry of m-TiO_2. Moreover, it might also be due to the presence of comparatively smaller number of Ti−O bonds, considering the inclusion of Cu_3VSe_4 nanocrystals in m-TiO_2.

Further, the XRD spectra of m-TiO_2 and Cu_3VSe_4/ m-TiO_2 films depicted in Figure S5 show the diffraction peaks at 25.40, 37.92, 48.1, 54.16, 54.60, 62.58, 68.94, 70.1, and 75.12° Bragg's angles corresponding to the (101), (004), (200), (105), (211), (204), (116), (220), and (215) crystal planes of the anatase phase of TiO_2.[42] The diffraction patterns of m-TiO_2 and

https://doi.org/10.1021/acsaem.4c00911
ACS Appl. Energy Mater. XXXX, XXX, XXX−XXX

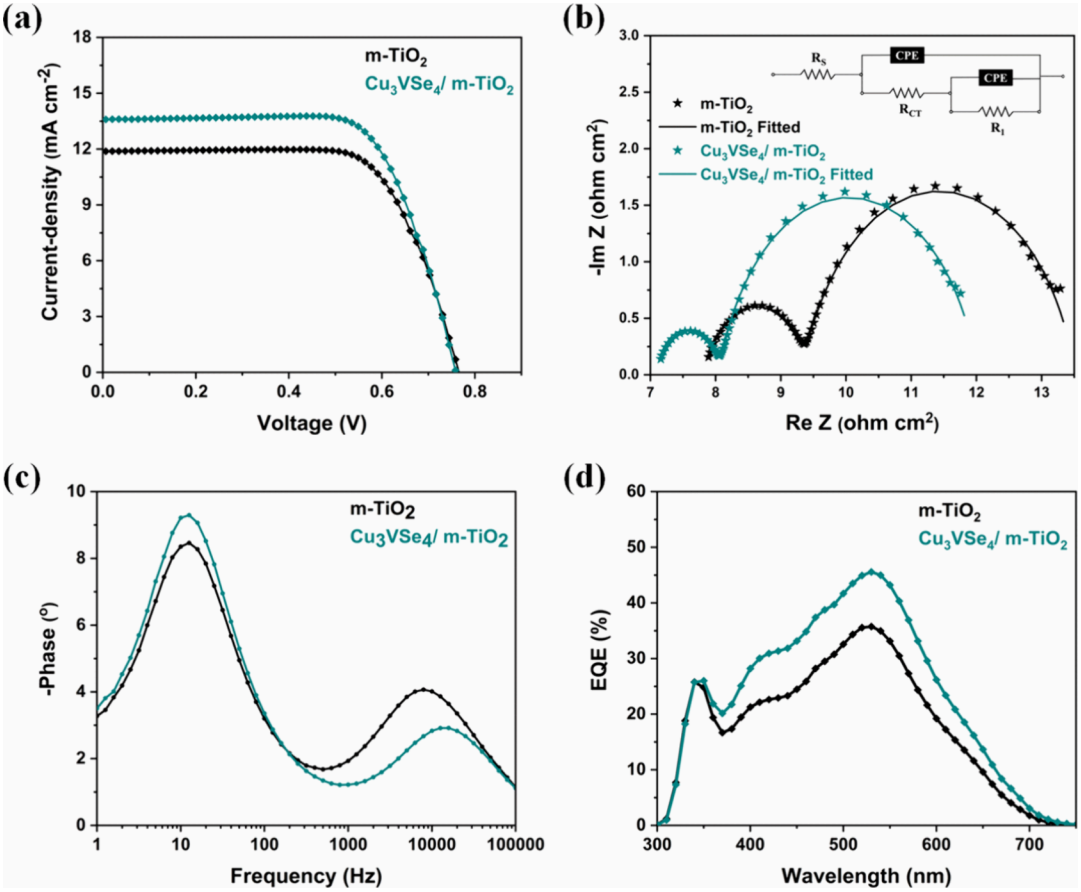

Figure 5. (a) Current density−voltage (J−V) characteristics. (b) Nyquist plots fitted with the equivalent circuit model (inset), where CPE is the constant phase element, R_S—series resistance, R_{CT}, and R_1−charge-transfer resistance at the CE/electrolyte and photoanode/electrolyte interfaces, respectively. (c) Bode plots and (d) EQE spectra of fabricated DSSC using m-TiO_2 and 0.045 w/w Cu_3VSe_4/m-TiO_2 photoanodes.

Cu_3VSe_4/ m-TiO_2 films match the database reference. No significant shift is observed in the diffraction spectra of Cu_3VSe_4/ m-TiO_2. This is potentially due to the small amount of Cu_3VSe_4 incorporation in m-TiO_2.

PV Characteristics and Charge-Transport Kinetics Investigations of Fabricated DSSCs. J−V plots of the reference m-TiO_2 and the optimized 0.045 w/w Cu_3VSe_4/m-TiO_2 photoanode-based DSSCs, as presented in Figure 5a, are used to quantify the PV parameters' improvement, as summarized in Table 2. Cu_3VSe_4/m-TiO_2 DSSCs showed an enhancement of 17.66% in J_{SC} with a negligible change in V_{OC} (0.001 V) compared to the reference m-TiO_2 DSSCs. The improved J_{SC} in Cu_3VSe_4/ m-TiO_2 DSSCs can be attributed to their enhanced light-harvesting capability. The incorporation of Cu_3VSe_4 nanocrystals plays a significant role in augmenting the absorbance of N719 dye-loaded Cu_3VSe_4/ m-TiO_2 photoanodes. Since Cu_3VSe_4 nanocrystals themselves absorb light within the visible spectrum, they complement the absorbance spectra of N719 dye molecules within the photoanodes. This synergistic effect resulted in an improved absorption of incident light in DSSCs. Consequently, this leads to the generation of a higher number of photogenerated charge carriers, thereby contributing to the observed increase in J_{SC}. Along with this, the slightly increased porosity of Cu_3VSe_4/m-TiO_2 observed in BET measurements might also contribute to improving light absorption via increasing the amount of N719 dye molecules adsorbed on the m-TiO_2 surface. It implies that comparatively more excitons could be generated under the light illumination. The higher the number of excitons, the higher is the number of photogenerated electrons, thus contributing to improved J_{SC}. The improved J_{SC} resulted in enhancement in the PCE of Cu_3VSe_4/m-TiO_2 DSSCs by 14.28% relative to the reference m-TiO_2 DSSCs. Considering the higher PL quenching and less recombination in the case of Cu_3VSe_4/m-TiO_2 photoanodes explained later, the highest J_{SC} can be defensible compared to m-TiO_2. Insignificant change in V_{OC} of m-TiO_2 and Cu_3VSe_4/m-TiO_2 implies balanced photogenerated electron injection from the sensitizer dye to the semiconductor and subsequent charge collection at the electrodes.

Table 2. PV Parameters of Fabricated DSSCs with Modified Photoanodes

photoanode	J_{SC} (mA cm^{-2})	V_{OC} (V)	FF	PCE (%) ± error[a]
m-TiO_2	11.55	0.760	0.72	6.37 ± 0.018
0.045 w/w Cu_3VSe_4/m-TiO_2	13.59	0.759	0.70	7.28 ± 0.072

[a]Based on five devices' analysis to estimate the error values.

The changes induced in the charge-transfer kinetics of modified photoanodes due to the influence of Cu_3VSe_4 on different interfacial layers of DSSCs are explained by electrochemical impedance spectroscopy (EIS). EIS measurements of all the fabricated DSSCs were taken under 1 sun illumination (100 mW cm^{-2}) within a frequency range of 0.1

https://doi.org/10.1021/acsaem.4c00911
ACS Appl. Energy Mater. XXXX, XXX, XXX−XXX

Hz to 1 MHz at the V_{OC} value of each device. Figure 5b shows the Nyquist plots of the m-TiO_2 and 0.045 w/w Cu_3VSe_4/m-TiO_2 DSSCs fitted with the equivalent circuit model (inset of Figure 5b). Two semicircles are seen in the Nyquist plots, which provide information in terms of charge-transfer resistances at different interfacial layers in DSSCs. R_{CT}, the charge-transfer resistance at the CE/electrolyte interface, is estimated from the diameter of high-frequency first semicircle. R_1, the charge-transfer resistance at the photoanode/electrolyte interface, is the diameter of the intermediate frequency second semicircle. Along with R_1 and R_{CT}, the series resistance (R_S) of the DSSCs, made up of contact resistance in different parts of the cell, CE bulk resistance, and FTO glass substrate resistance, is determined from the high-frequency semicircle intercept on the Re Z x-axis. The obtained EIS parameters for all of the fabricated DSSCs are summarized in Table 3. It is seen that the resistances at different interfacial layers (R_{CT}, R_1, and R_S) reduced in Cu_3VSe_4/m-TiO_2 DSSC relative to the reference m-TiO_2 photoanode. The smaller diameter of semicircles representing reduced resistances indicates faster photogenerated electron transfer throughout the different interfaces in DSSCs. A slight reduction in R_1 represents comparatively lesser recombination reactions at the photoanode/electrolyte interface, which matches the PL investigation explained later. Further, reduced R_{CT} indicates faster reduction of I_3^- to I^- ions at the CE/electrolyte interface, resulting in comparatively faster regeneration of N719 dye molecules through electrons produced during the oxidation of I^- to I_3^- ions.

Table 3. EIS Parameters of Fabricated DSSCs with Modified Photoanodes

photoanode	R_S (Ω cm^2)	R_{CT} (Ω cm^2)	R_1 (Ω cm^2)	τ (ms)
m-TiO_2	7.89	1.46	3.78	12.64
0.045 w/w Cu_3VSe_4/m-TiO_2	7.16	0.89	3.70	12.64

Figure 5c shows the Bode plots of fabricated DSSCs and provides an estimated value of the photogenerated electron lifetime (τ) at the photoanode/electrolyte interface using the frequency maxima (f_{max}) of the lower frequency peak in the equation, $\tau = {}^{1}/_{2\pi f_{max}}$. Since f_{max} of the first peak (low frequency) in the Bode plot of Cu_3VSe_4/m-TiO_2 photoanode-based DSSCs remains almost the same, it signifies no change in the photogenerated electron lifetime at the photoanode/electrolyte interface (~12.64 ms), which corroborates with the negligible change in the R_1 value. Moreover, a shift in f_{max} of the second peak toward a higher frequency indicates a reduction in the photogenerated electron lifetime at the CE/electrolyte interface. The reduced electron lifetime at the CE/electrolyte interface along with the significantly reduced R_{CT} value further facilitates the faster charge transport in DSSCs. Hence, this confirms the faster and better charge-transfer kinetics of DSSCs with the incorporation of Cu_3VSe_4 nanocrystals in m-TiO_2.

The external quantum efficiency (EQE) spectrum associated with the fabricated DSSCs without and with Cu_3VSe_4-incorporated m-TiO_2 photoanodes is depicted in Figure 5d.

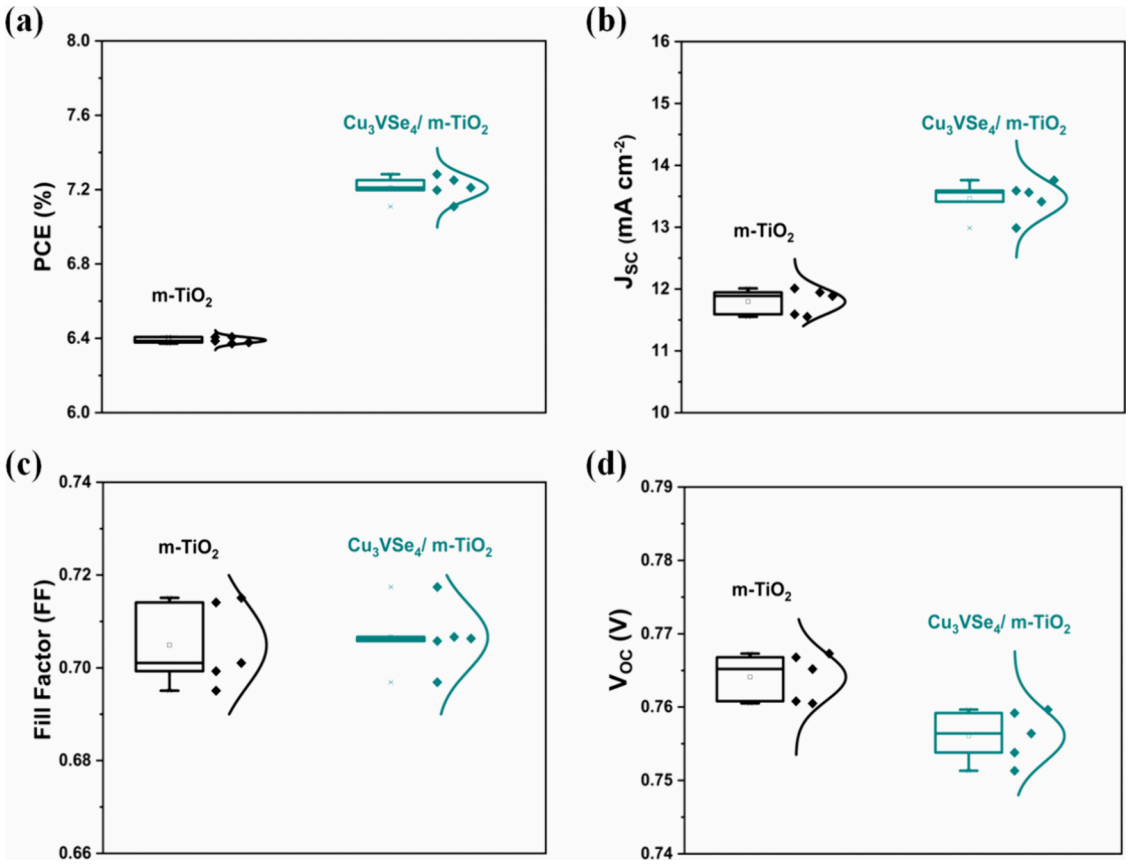

Figure 6. Box plots displaying (a) PCE, (b) J_{SC}, (c) FF, and (d) V_{OC} of five sets of fabricated DSSCs using m-TiO_2 (black) and 0.045 w/w Cu_3VSe_4/m-TiO_2 photoanodes (dark cyan).

https://doi.org/10.1021/acsaem.4c00911
ACS Appl. Energy Mater. XXXX, XXX, XXX−XXX

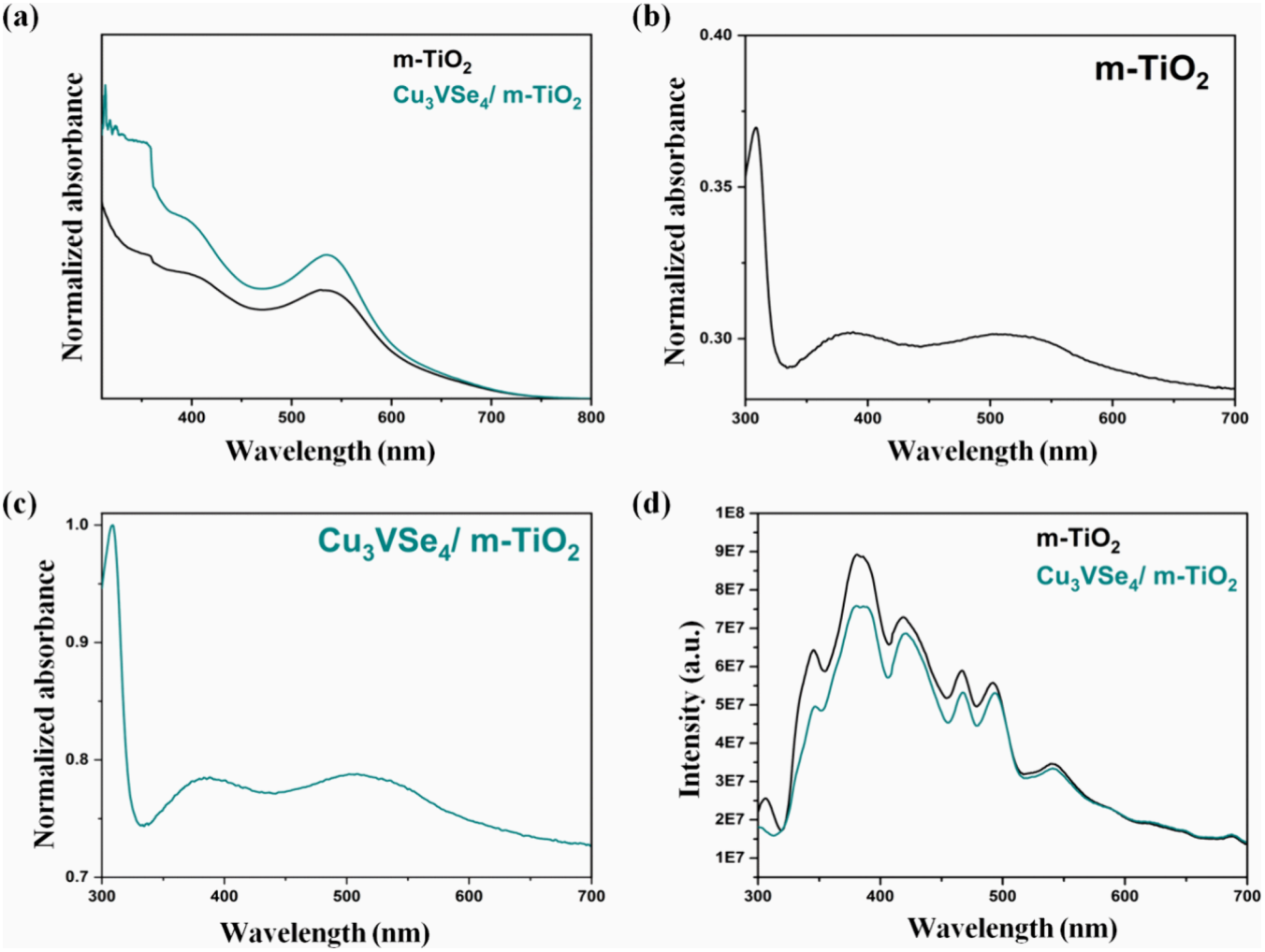

Figure 7. (a) UV absorbance spectra of N719 dye-loaded m-TiO_2 and Cu_3VSe_4/m-TiO_2 photoanodes, and dye deloaded from (b) TiO_2 and (c) Cu_3VSe_4/m-TiO_2. (d) PL spectra of m-TiO_2 and Cu_3VSe_4/m-TiO_2 (0.045 w/w).

In typical DSSCs, EQE is the ratio of the number of charge carriers collected by the electrodes to the number of incident photons and hence determines the ability to generate electrons per unit incident photons. The mathematical expression of EQE value is a representation of various factors occurring in DSSCs and is given by eq 1

$$\mathrm{EQE} = \mathrm{LHE}(\lambda).\ \phi_{\mathrm{inj}}.\ \phi_{\mathrm{col}} \tag{1}$$

where $\mathrm{LHE}(\lambda)$ is the photon-harvesting efficiency, ϕ_{inj} is the quantum yield which represents the electron injection from the excited dye molecules, and ϕ_{col} is the charge-collecting efficiency representing the charge transfer to the photoanode.

EQE spectrum of both the fabricated DSSCs showed a photoresponse within the wavelength spectrum from 320 to 700 nm and is in agreement with the UV−visible absorption spectrum of N719 dye-loaded TiO_2 photoanodes shown later. Similar to the absorbance spectra, it is evident that the 0.045 w/w Cu_3VSe_4/m-TiO_2 DSSCs exhibited better photoresponse in comparison to m-TiO_2 DSSC. EQE peak value appears at 530 nm, where Cu_3VSe_4/m-TiO_2 DSSC showed a 45.56% value, comparatively higher than m-TiO_2 DSSC (35.75%). It, thus, confirms that the incorporation of Cu_3VSe_4 nanocrystals in m-TiO_2 photoanodes enhances the number of electron−hole pair generation in the visible region of the electromagnetic spectrum contributing to ϕ_{inj} and ϕ_{col}. The higher number of electron pair generation in Cu_3VSe_4/m-TiO_2 DSSC thus led to higher J_{SC} and hence PCE. Therefore, Cu_3VSe_4/m-TiO_2 DSSC recorded relatively enhanced EQE spectra than m-TiO_2 DSSC. The EQE spectrum of m-TiO_2 and 0.055, 0.045, and 0.035 w/w Cu_3VSe_4/m-TiO_2 DSSCs is depicted in Figure S6, exhibiting EQE values at 530 nm to be 35.75, 44.70, 45.56, and 42.84% which agrees well with the PV parameters obtained from their respective $J-V$ curves (SI).

To ascertain the repeatability and reproducibility of the Cu_3VSe_4-modified photoanodes in DSSCs, five sets of DSSCs were fabricated with and without Cu_3VSe_4 incorporation. The statistics of the fabricated m-TiO_2 DSSC and 0.045 w/w Cu_3VSe_4/m-TiO_2 DSSCs with respect to the obtained PV parameters are represented in the form of Box plots (Figure 6) displaying their PCE, J_{SC}, FF, and V_{OC}. Along with this, the reproducibility curve depicted in Figure S7 with the error bar in the PCE of fabricated DSSCs showed the consistency in the obtained results.

Improved Light-Harvesting Investigations. To confirm the improved light-harvesting ability of photoanodes of Cu_3VSe_4-incorporated m-TiO_2 DSSCs, the UV−visible absorbance spectra of N719 dye loaded and deloaded from doctor-bladed m-TiO_2 and Cu_3VSe_4/m-TiO_2 films were collected. To mitigate potential variations in the impact of

https://doi.org/10.1021/acsaem.4c00911
ACS Appl. Energy Mater. XXXX, XXX, XXX−XXX

photoanode thickness on adsorbed dye molecules and the PV characteristics of DSSC devices, both films were fabricated with nearly identical active areas of 0.15 cm^2 and a thickness of approximately 11.5 μm. N719 dye-loaded film samples of m-TiO_2 and Cu_3VSe_4/m-TiO_2 deposited on FTO substrates were used to obtain the absorbance spectra depicted in Figure 7a. A significant increase in the absorbance of N719 dye-loaded Cu_3VSe_4/m-TiO_2 is observed relative to dye-loaded m-TiO_2, with broadened peaks around 393 and 533 nm, which are the characteristic peaks of N719 dye molecules related to metal-to-ligand charge-transfer transitions between the π orbitals of Ru (II) and π^* orbitals of bipyridine carboxylate.[43,44] The overlapping of absorbance peaks of Cu_3VSe_4 nanocrystals within the 300−800 nm range and N719 dye molecules within the 350−600 nm range resulted in improved overall absorbance, hence improving the light harvesting of photoanodes, leading to improved PV performance of Cu_3VSe_4/m-TiO_2 DSSCs.

Considering the slightly improved porosity of Cu_3VSe_4/m-TiO_2, the N719 dye loading content increased. It is further confirmed from the UV−visible absorbance spectra of dye deloaded from m-TiO_2 and Cu_3VSe_4/m-TiO_2 presented in Figure 7b,c. Dye deloading is performed by dipping the N719 dye-loaded m-TiO_2 and Cu_3VSe_4/m-TiO_2 films in a 0.1 M aqueous solution of potassium hydroxide (KOH) for forced dye desorption. The resulting spectra exhibited a sharp absorption band in the UV region at 307 nm and two broadened bands around 380 and 530 nm in the visible region, related to the ligand-centered charge-transfer transitions and metal-to-ligand charge-transfer transitions of N719 dye molecules, respectively. Along with this, an increase in the absorbance of N719 dye deloaded from Cu_3VSe_4/m-TiO_2 photoanodes is observed in comparison to m-TiO_2. The amount of dye loaded on the m-TiO_2 and Cu_3VSe_4/m-TiO_2 photoanodes can be estimated from eq 2

$$\text{Dyedeloading (mol cm}^{-2}) = \frac{\text{Dye concentration (M)} \times V\ \text{(mL)}}{\text{Electrodearea (cm}^2)} \quad (2)$$

where V is the volume of the solution taken for each measurement which is 3 mL, dye concentration is calculated using Beer−Lambert's law at the absorbance value around 530 nm, and effective area is taken as 0.15 cm^2. The dye loading amount is calculated to be around 0.62 and 1.62 mol cm^{-2} for m-TiO_2 and Cu_3VSe_4/m-TiO_2, respectively.

Insights to Reduced Recombination Reactions at the Photoanode/Electrolyte Interface in Modified DSSCs. To get better insights on the improved charge transfer and slightly reduced charge carrier recombination processes in Cu_3VSe_4/m-TiO_2 DSSC, PL emission spectra of doctor-bladed m-TiO_2 and Cu_3VSe_4/m-TiO_2 films (Figure 7d) were obtained at an excitation wavelength of 280 nm. PL emission spectra arise due to the luminescence from localized surface states, i.e., nonirradiative processes of m-TiO_2 during the recombination of photogenerated electron−hole pairs. Thus, lower PL intensity represents lesser recombination rate. In both the samples, broad emission peaks within the range 320−580 nm were observed, however, with a decrease in the PL intensity for Cu_3VSe_4/m-TiO_2 relative to m-TiO_2. The peaks around 423, 461, 485, and 527 nm are attributed to the presence of formation of intrinsic oxygen vacancies in m-TiO_2, anatase phase of m-TiO_2, and the transition of two trapped and one trapped electron from the oxygen vacancies to the valence band (VB) of m-TiO_2. For the electron−hole recombination process, the photogenerated electrons could be transferred first from the CB to the oxygen vacancies (nonradiative process) and then to the VB (fluorescence emission) of m-TiO_2. The decrease in the PL intensity of Cu_3VSe_4/m-TiO_2 than m-TiO_2 indicates that the transition of electrons from the CB of m-TiO_2 to the oxygen vacancies is suppressed by the creation of new energy levels through Cu_3VSe_4 incorporation. The surface energy level of Cu_3VSe_4 might be positioned between the CB of m-TiO_2 and the energy level of intrinsic oxygen vacancies. It is indicative of better change-transport processes occurring at the photoanode/electrolyte interface of fabricated Cu_3VSe_4/m-TiO_2 DSSC and hence their improved PV performance.[45]

CONCLUSIONS

The present study validates the Cu_3VSe_4 nanocrystals' positive impact on the light-harvesting capability of m-TiO_2 and demonstrated a substantial enhancement in the PV performance of Cu_3VSe_4/m-TiO_2 DSSCs. When Cu_3VSe_4 nanocrystals were incorporated into m-TiO_2, they resulted in a significant improvement in the J_{SC} and PCE values of 17.66 and 14.28% in DSSCs compared to the reference m-TiO_2 DSSCs. The enhancement is a result of synergy between various factors as follows. The presence of Cu_3VSe_4 nanocrystals in m-TiO_2 contributed to an improved charge-transfer kinetics in DSSCs, explained by the reduced resistances at different interfacial layers in DSSCs as compared to the reference m-TiO_2 DSSC. Furthermore, the increased specific surface area and porosity of m-TiO_2 achieved through the incorporation of Cu_3VSe_4 nanocrystals are estimated from the BET measurements. The enhanced porosity facilitated higher dye loading content, leading to an increased number of photogenerated electrons and, consequently, an enhancement in the J_{SC} of Cu_3VSe_4/m-TiO_2 DSSCs. The improved PV performance of Cu_3VSe_4/m-TiO_2 DSSCs is confirmed by the significantly improved spectral photoresponse (45.56%) relative to m-TiO_2 DSSC (35.75%) obtained from the EQE study. Henceforth, the nanocrystals of Cu_3VSe_4 not only exhibit the capacity to enhance the light-harvesting efficiency of DSSCs but also present promising benefits for the forthcoming generations of PV devices.

ASSOCIATED CONTENT

Supporting Information

The Supporting Information is available free of charge at https://pubs.acs.org/doi/10.1021/acsaem.4c00911.

$J-V$ characteristic curves of fabricated DSSC with varied amounts of Cu_3VSe_4 (0.055, 0.045, 0.035 w/w) incorporated m-TiO_2-based photoanodes; PV parameters of fabricated DSSCs with varied amounts of Cu_3VSe_4 incorporated m-TiO_2-based photoanodes; EDS spectra and the respective elemental mapping of m-TiO_2 thin film; EDS spectra and the respective elemental mapping of optimized 0.045 w/w Cu_3VSe_4/m-TiO_2 films; nitrogen (N_2) adsorption−desorption isotherms and cumulative and differential pore volume distribution of m-TiO_2 and optimized 0.045 w/w Cu_3VSe_4/ m-TiO_2 films; XRD pattern of m-TiO_2 and optimized 0.045 w/w Cu_3VSe_4/ m-TiO_2 films; EQE spectra of fabricated DSSC using m-TiO_2 and with varied amounts of Cu_3VSe_4 (0.055, 0.045, and 0.035 w/

https://doi.org/10.1021/acsaem.4c00911
ACS Appl. Energy Mater. XXXX, XXX, XXX−XXX

w)-incorporated m-TiO_2-based photoanodes; and reproducibility curves of fabricated m-TiO_2 and 0.045 w/w Cu_3VSe_4/m-TiO_2 photoanode-based DSSCs (PDF)

AUTHOR INFORMATION

Corresponding Author

Daniela R. Radu − *Department of Mechanical and Materials Engineering, Florida International University, Miami, Florida 33174, United States;* orcid.org/0000-0001-6833-5825; Email: dradu@fiu.edu

Authors

Navdeep Kaur − *Department of Mechanical and Materials Engineering, Florida International University, Miami, Florida 33174, United States;* orcid.org/0000-0002-4140-1535

Linisha Biswal − *Department of Mechanical and Materials Engineering, Florida International University, Miami, Florida 33174, United States*

Alexander Prieto − *Department of Mechanical and Materials Engineering, Florida International University, Miami, Florida 33174, United States*

Cheng-Yu Lai − *Department of Mechanical and Materials Engineering, Florida International University, Miami, Florida 33174, United States; Department of Chemistry and Biochemistry, Florida International University, Florida, Miami 33199, United States;* orcid.org/0000-0002-8931-5601

Complete contact information is available at: https://pubs.acs.org/10.1021/acsaem.4c00911

Author Contributions

N.K. and L.B. contributed equally. The manuscript was written through the contributions of all authors. All authors have given approval to the final version of the manuscript.

Notes

The authors declare no competing financial interest.

ACKNOWLEDGMENTS

This work was supported in part by the National Science Foundation Award # DMR-2122078, NASA Award # 80NSSC19M0201, and Department of Defense Awards # W911NF2210186 and W911NF2310152. L.B. and A.P. were supported by NASA Award # 80NSSC19M0201, and N.K by NSF DMR-2122078. The authors thank Jake Carrier, Dr. Chen Yu-Chang, and Dr. Sahil Gasso for their help in collecting BET, TEM, and PL data, respectively.

REFERENCES

(1) Sayah, D.; Ghaddar, T. H. Investigation of Ethylisopropyl Sulfone Medium with a Copper-Based Redox Electrolyte for Ambient Light Dye-Sensitized Solar Cells: Achieving High Efficiency and Enduring Long-Term Stability. *ACS Applied Energy Materials* **2023**, *6* (23), 11924−33.

(2) Juang, S.S.-Y.; Lin, P.-Y.; Lin, Y.-C.; Chen, Y.-S.; Shen, P.-S.; Guo, Y.-L.; Wu, Y.-C.; Chen, P. Energy harvesting under dim-light condition with dye-sensitized and perovskite solar cells. *Frontiers in Chemistry* **2019**, *7*, 209.

(3) Kim, J. H.; Moon, K. J.; Kim, J. M.; Lee, D.; Kim, S. H. Effects of various light-intensity and temperature environments on the photovoltaic performance of dye-sensitized solar cells. *Sol. Energy* **2015**, *113*, 251−7.

(4) Chalgynbayeva, A.; Gabnai, Z.; Lengyel, P.; Pestisha, A.; Bai, A. Worldwide research trends in agrivoltaic systems—a bibliometric review. *Energies* **2023**, *16* (2), 611.

(5) Roslan, N.; Yaacob, M.; Jamaludin, D.; Hashimoto, Y.; Othman, M.; Iskandar, A. N.; Ariffin, M.; Ibrahim, M.; Mailan, J.; Jamaluddin, A. Dye-Sensitized Solar Cell (DSSC): Effects on Light Quality, Microclimate, and Growth of Orthosiphon stamineus in Tropical Climatic Condition. *Agronomy* **2021**, *11* (4), 631.

(6) Rahman, S.; Haleem, A.; Siddiq, M.; Hussain, M. K.; Qamar, S.; Hameed, S.; Waris, M. Research on dye sensitized solar cells: recent advancement toward the various constituents of dye sensitized solar cells for efficiency enhancement and future prospects. *RSC Adv.* **2023**, *13* (28), 19508−29.

(7) Kumar, Y.; Chhalodia, T.; Bedi, P. K. G.; Meena, P. Photoanode modified with nanostructures for efficiency enhancement in DSSC: a review. *Carbon Letters* **2023**, *33* (1), 35−58.

(8) Yeoh, M.-E.; Chan, K.-Y.; Wong, H.-Y.; Thien, G. S. H.; Low, P.-L.; Ng, Z.-N.; Murthy, H. A.; Balachandran, R. A novel simplified approach in fabricating TiO_2 photoanodes for dye-sensitized solar cells. *Mater. Lett.* **2023**, *349*, No. 134730.

(9) Fegade, U.; Conghao, C.; Chen, Y.-J.; Alshahrani, T.; Khan, F.; Afzaal, M.; Wu, R.-J.; Al-Ahmed, A. Comparative analysis of the photovoltaic cell parameters of dye-sensitized solar cells with composite photoanodes: Effect of the alien component. *Opt. Mater.* **2023**, *143*, No. 114109.

(10) Nizamudeen, C.; Krishnapriya, R.; Mozumder, M.; Mourad, A. I.; Ramachandran, T. Photovoltaic performance of MOF-derived transition metal doped titania-based photoanodes for DSSCs. *Sci. Rep.* **2023**, *13* (1), 6345.

(11) Kabir, D.; Forhad, T.; Ghann, W.; Richards, B.; Rahman, M. M.; Uddin, M. N.; Rakib, M. R. J.; Shariare, M. H.; Chowdhury, F. I.; Rabbani, M. M. Dye-sensitized solar cell with plasmonic gold nanoparticles modified photoanode. *Nano-Struct. Nano-Obj.* **2021**, *26*, No. 100698.

(12) Shamsudin, N.; Shafie, S.; Ab Kadir, M. A.; Ahmad, F.; Sulaiman, Y.; Chachuli, S.; Razali, M. Flexible back-illuminated dye sensitised solar cells (DSSCs) with titanium dioxide/silver nanoparticles composite photoanode for improvement of power conversion efficiency. *Optik* **2023**, *272*, No. 170237.

(13) Ahmad, I.; Jafer, R.; Abbas, S. M.; Ahmad, N.; Iqbal, J.; Bashir, S.; Melaibari, A. A.; Khan, M. H. Improving energy harvesting efficiency of dye sensitized solar cell by using cobalt-rGO co-doped TiO_2 photoanode. *J. Alloys Compd.* **2022**, *891*, No. 162040.

(14) Chou, J.-C.; Chen, P.-F.; Yang, P.-H.; Lai, C.-H.; Kuo, P.-Y.; Nien, Y.-H.; Syu, R.-H.; Wu, Y.-T.; Zhuang, S.-W. Modifications to the Scattering Layer of a Dye-Sensitized Solar Cell Photoanode With Bifunctional WO_3 Hollow Spheres for Increased Electron Transfer and Scattering Effect. *IEEE Trans. Electron Devices* **2023**, *70* (5), 2415−23.

(15) Mahmoudi, M.; Alizadeh, A.; Roudgar-Amoli, M.; Shariatinia, Z. Rational modification of TiO_2 photoelectrodes with spinel $ZnFe_2O_4$ and Ag-doped $ZnFe_2O_4$ nanostructures highly enhanced the efficiencies of dye sensitized solar cells. *Spectrochimica Acta Part A: Molecular and Biomolecular Spectroscopy* **2023**, *289*, No. 122214.

(16) Chinnarani, M.; Suresh, S.; Prabu, K.; Kandasamy, M.; Pugazhenthiran, N. Facile synthesis of reduced graphene oxide and graphitic carbon nitride modified titanium dioxide nanospheres for photoanode of dye-sensitized solar cell. *Inorg. Chim. Acta* **2024**, *560*, No. 121842.

(17) Nien, Y.-H.; Wu, Y.-T.; Chou, J.-C.; Yang, P.-H.; Ho, C.-S.; Lai, C.-H.; Kuo, P.-Y.; Syu, R.-H.; Zhuang, S.-W.; Chen, P.-F. Photovoltaic Performance of Dye-Sensitized Solar Cell by Modification of Photoanode With $PbTiO_3$−$ZnFe_2O_4$/TiO_2 Nanofibers. *IEEE Trans. Electron Devices* **2023**, *70* (7), 3780−7.

(18) Chou, J.-C.; Lin, Y.-C.; Lai, C.-H.; Kuo, P.-Y.; Nien, Y.-H.; Chang, J.-X.; Hu, G.-M.; Yong, Z.-R. Electron Conduction Channel of Silver Nanowire Modified TiO_2 Photoanode for Improvement of Interface Impedance of Dye-Sensitized Solar Cell. *IEEE Journal of the Electron Devices Society* **2021**, *9*, 250−6.

(19) Imani, S.; Alizadeh, A.; Roudgar-Amoli, M.; Shariatinia, Z. Bi-layered photoelectrodes of TiO_2/activated carbon modified with $SrTiO_3$ films boosted sunlight harvesting of dye-sensitized solar cells. *Inorg. Chem. Commun.* **2022**, *145*, No. 110045.
(20) Kanjana, N.; Maiaugree, W.; Poolcharuansin, P.; Laokul, P. Synthesis and characterization of Fe-doped TiO_2 hollow spheres for dye-sensitized solar cell applications. *Materials Science and Engineering: B* **2021**, *271*, No. 115311.
(21) Prajapati, N.; Murthy, C.; Machhi, H. K.; Soni, S. S. A novel f-MWCNT-based nanocomposite for enhancement of photoconversion efficiency of DSSC. *Journal of Materials Science: Materials in Electronics* **2023**, *34* (32), 2129.
(22) Peiris, D.; Ekanayake, P.; Karunaratne, B.; Petra, M. I. Improved performance of DSSC photoanodes after the modification of TiO_2 with reduced graphene oxide. *J. Electron. Mater.* **2021**, *50*, 1044−53.
(23) Sahu, K.; Dhonde, M.; Murty, V. V. S. Microwave-assisted hydrothermal synthesis of Cu-doped TiO_2 nanoparticles for efficient dye-sensitized solar cell with improved open-circuit voltage. *International Journal of Energy Research* **2021**, *45* (4), 5423−32.
(24) Shobana, M.; Balraju, P.; Muthukumarasamy, N.; Velauthapillai, D. Glycerol-supportive Y^{3+} infused TiO_2 nanoparticles: An electrode material for dye sensitized solar cell and supercapacitor applications. *Journal of Energy Storage* **2023**, *73*, No. 108943.
(25) Chang, C.-Y.; Prado-Rivera, R.; Liu, M.; Lai, C.-Y.; Radu, D. R. Colloidal synthesis and photocatalytic properties of Cu_3NbS_4 and Cu_3NbSe_4 sulvanite nanocrystals. *ACS Nanoscience Au* **2022**, *2* (5), 440−7.
(26) Liu, M.; Lai, C.-Y.; Chang, C.-Y.; Radu, D. R. Solution-Based Synthesis of Sulvanite Cu_3TaS_4 and Cu_3TaSe_4 Nanocrystals. *Crystals* **2021**, *11* (1), 51.
(27) Prado-Rivera, R.; Chang, C.-Y.; Liu, M.; Lai, C.-Y.; Radu, D. R. Sulvanites: The Promise at the Nanoscale. *Nanomaterials* **2021**, *11* (3), 823.
(28) Chen, C.-C.; Stone, K. H.; Lai, C.-Y.; Dobson, K. D.; Radu, D. Sulvanite (Cu_3VS_4) nanocrystals for printable thin film photovoltaics. *Mater. Lett.* **2018**, *211*, 179−82.
(29) Zhao, Y.; Liu, M.; Zhang, W.; Sun, X.; Wang, W.; Zhang, W.; Tang, M.; Ren, W.; Sun, M.; Feng, W. Solution-phase controlled synthesis of Cu_3NbSe_4 nanocrystals for optoelectronic applications. *Dalton Trans.* **2022**, *51* (44), 16937−16944.
(30) Chang, C.-Y.; Kaur, N.; Prado-Rivera, R.; Lai, C.-Y.; Radu, D. Size-Controlled Cu_3VSe_4 Nanocrystals as Cathode Material in Platinum-Free Dye-Sensitized Solar Cells. *ACS Appl. Mater. Interfaces* **2024**, *16*, 13719.
(31) Kaur, N.; Oyon, S. A.; Lai, C.-Y.; Radu, D. R. From reflection to absorption: Improving light harvesting of dye sensitized solar cells with Cu nanowires as reflectors. *Opt. Mater.* **2023**, *142*, No. 114074.
(32) Fina, J.; Kaur, N.; Chang, C.-Y.; Lai, C.-Y.; Radu, D. R. Enhancing Light Harvesting in Dye-Sensitized Solar Cells through Mesoporous Silica Nanoparticle-Mediated Diffuse Scattering Back Reflectors. *Electron. Mater.* **2023**, *4*, 124−135, DOI: 10.3390/electronicmat4030010.
(33) Liu, M.; Lai, C.-Y.; Selopal, G. S.; Radu, D. R. Synthesis and optoelectronic properties of Cu_3VSe_4 nanocrystals. *PLoS One* **2020**, *15* (5), No. e0232184.
(34) Liu, M.; Lai, C.-Y.; Zhang, M.; Radu, D. R. Cascade synthesis and optoelectronic applications of intermediate bandgap Cu_3VSe_4 nanosheets. *Sci. Rep.* **2020**, *10* (1), 21679.
(35) Schmidt, K.; Müller, A.; Bouwma, J.; Jellinek, F. Übergangsmetall-chalklogen-verbindungen IR-und raman-spektren von Cu_3Mx_4 (m= v, nb, ta; x= s, se). *J. Mol. Struct.* **1972**, *11* (2), 275−82.
(36) Mantella, V.; Ninova, S.; Saris, S.; Loiudice, A.; Aschauer, U.; Buonsanti, R. Synthesis and size-dependent optical properties of intermediate band gap Cu_3VS_4 nanocrystals. *Chem. Mater.* **2019**, *31* (2), 532−40.
(37) Kaur, N.; Syed, F. M.; Fina, J.; Lai, C.-Y.; Radu, D. R. Ag reflectors: an effective approach to improve light harvesting in dye sensitized solar cells. *IEEE Journal of Photovoltaics* **2023**, *13* (2), 250−3.
(38) Subalakshmi, K.; Senthilselvan, J. Effect of fluorine-doped TiO2 photoanode on electron transport, recombination dynamics and improved DSSC efficiency. *Sol. Energy* **2018**, *171*, 914−28.
(39) Al-Amin, M.; Dey, S. C.; Rashid, T. U.; Ashaduzzaman, M.; Shamsuddin, S. M. Solar assisted photocatalytic degradation of reactive azo dyes in presence of anatase titanium dioxide. *Int. J. Latest Res. Eng. Technol.* **2016**, *2* (3), 14−21.
(40) Liu, H.; Wang, A.; Sun, Q.; Wang, T.; Zeng, H. Cu nanoparticles/fluorine-doped tin oxide (FTO) nanocomposites for photocatalytic H_2 evolution under visible light irradiation. *Catalysts* **2017**, *7* (12), 385.
(41) Kaur, N.; Mahajan, A.; Bhullar, V.; Singh, D. P.; Saxena, V.; Debnath, A. K.; Aswal, D. K.; Devi, D.; Singh, F.; Chopra, S. Fabrication of plasmonic dye-sensitized solar cells using ion-implanted photoanodes. *RSC Adv.* **2019**, *9* (35), 20375−84.
(42) El Bendali, A.; Aqil, M.; Hdidou, L.; El Halya, N.; El Ouardi, K.; Alami, J.; Boschetto, D.; Dahbi, M. The Electrochemical and Structural Changes of Phosphorus-Doped TiO_2 through In Situ Raman and In Situ X-Ray Diffraction Analysis. *ACS Omega* **2024**, *9* (13), 14911−22.
(43) Kaur, N.; Bhullar, V.; Singh, D. P.; Mahajan, A. Bimetallic Implanted Plasmonic Photoanodes for TiO_2 Sensitized Third Generation Solar Cells. *Sci. Rep.* **2020**, *10* (1), 7657.
(44) Awasthi, K.; Hsu, H.-Y.; Diau, E.W.-G.; Ohta, N. Enhanced charge transfer character of photoexcited states of dye sensitizer on the N719/TiO2 interface as revealed by electroabsorption spectra. *J. Photochem. Photobiol., A* **2014**, *288*, 70−5.
(45) Kumaravel, V.; Rhatigan, S.; Mathew, S.; Bartlett, J.; Nolan, M.; Hinder, S. J.; Sharma, P. K.; Singh, A.; Byrne, J. A.; Harrison, J. Indium-doped TiO_2 photocatalysts with high-temperature anatase stability. *J. Phys. Chem. C* **2019**, *123* (34), 21083−21096.

https://doi.org/10.1021/acsaem.4c00911
ACS Appl. Energy Mater. XXXX, XXX, XXX−XXX